Effect of Anisotropic Permeability on Band Growth

Jesse Taylor-West

October 17, 2014

1 Introduction

The mechanics of partially molten regions of the mantle are not well understood- in part due to the inaccessibility of these regions to observation. However it is widely agreed that experiments performed on synthetic mantle rocks [e.g King et al., 2010] act as a reasonable test of theoretical models of magma dynamics. One consistently observed feature of experiments on partially molten mantle rocks deformed under strain is the emergence of high-porosity bands at angles between 15° and 20° to the shear plane.

A number of theoretical approaches have been made to reproduce the formation of these low angle bands in models. The most recent of these, for example by Katz and Takei [2013], have involved the inclusion of anisotropic viscosity arising from the grain-scale distribution of melt, as formulated by Takei and Holtzman [2009]. It is reasonable to assume that the melt-preffered orientation (MPO) may also lead to anisotropy in permeability- the effects of which are unexplored. In this project I investigate the impact of anisotropic permeability on the dynamics of partially molten rock, specifically on its role in low-angle band formation in deformation under simple shear.

2 Governing Equations

2.1 Conservation statements

The two-phase flow theory involves the evolution of liquid volume fraction ϕ, liquid velocity $\boldsymbol{v}^L$, liquid pressure p^L, matrix velocity $\boldsymbol{v}^S$ and the average stress of the two-phase aggregate, σ_{ij}. These are related by mass conservation equations for the liquid and solid phases and momentum conservation equations for the liquid phase and the bulk mixture.

$$\frac{\partial \rho^L \phi}{\partial t} + \nabla \cdot \left[\rho^L \phi \boldsymbol{v}^L \right] = \Gamma, \tag{1a}$$

$$\frac{\partial \rho^S (1 - \phi)}{\partial t} + \nabla \cdot \left[\rho^S (1 - \phi) \boldsymbol{v}^S \right] = -\Gamma, \tag{1b}$$

$$\frac{1}{\eta^L} \mathbf{K} \left[\nabla p^L - \rho^L \boldsymbol{g} \right] = \phi \left(\boldsymbol{v}^S - \boldsymbol{v}^L \right), \tag{1c}$$

$$\left[\sigma_{ij} + p^L \delta_{ij} \right]_{,j} + \bar{\rho} g_i = p^L_{,i}, \tag{1d}$$

where ρ^L and ρ^S are the densities of liquid and matrix respectively, $\bar{\rho} = (1 - \phi)\rho^S + \phi \rho^L$ is the average aggregate density, Γ is the melting rate, $\boldsymbol{g}$ is the gravitational acceleration and η^L is the liquid viscosity. Allowing for anisotropic permeability, $\mathbf{K}$ is a tensor rather than a scalar. We assume no melting, and the solid and liquid densities are constant and equal ($\rho^L = \rho^S = \rho$).
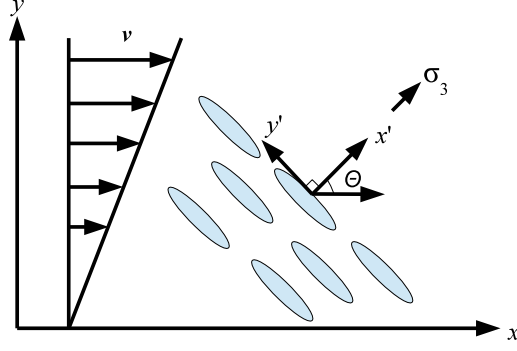
Figure 1: Background simple-shear flow, $\boldsymbol{v}$, and melt pocket allignment due to applied stress

2.2 Constitutive relations

To close the system of partial differential equations (1) requires the specification of constitutive relations between stress and strain, and between permeability $\mathbf{K}$ and porosity ϕ. We use the Newtonian, isotropic viscous constitutive relation between stress, σ_{ij}, and strain of the matrix, $\dot{\varepsilon}_{ij} = (v^S_{i,j} + v^S_{j,i})/2$. The permeability tensor, $\mathbf{K} = \mathbf{K}(\phi)$, is given by the closure condition

$$\mathbf{K}(\phi) = K_0 \left(\frac{\phi}{\phi_0} \right)^n \mathbf{A} \tag{2}$$

where n is a constant, usually taken as two or three, ϕ_0 is a reference porosity, K_0 is a reference scalar permeability and $\mathbf{A}$ is a non-dimensional tensor determined by the form of the permeability anisotropy (note that $\mathbf{A}$ could depend on other variables, particularly stress σ_{ij} which can cause MPO).

Then the four equations (1) can be combined to eliminate $\boldsymbol{v}^L$ (and denote matrix velocity as $\boldsymbol{v}$), resulting in the system

$$\frac{\partial \phi}{\partial t} = \nabla \cdot \left[(1 - \phi)\boldsymbol{v} \right], \tag{3a}$$

$$\nabla \cdot \boldsymbol{v} = \nabla \cdot \left[\frac{1}{\eta^L} \mathbf{K} \left(\nabla p^L - \rho \boldsymbol{g} \right) \right], \tag{3b}$$

$$\nabla p^L = \nabla \cdot \left[\eta (\nabla \boldsymbol{v} + \nabla \boldsymbol{v}^T) \right] + \nabla \left[\left(\xi - \frac{2}{3}\eta \right) \nabla \cdot \boldsymbol{v} \right] + \rho \boldsymbol{g}, \tag{3c}$$

where η and ξ correspond to the shear and bulk viscosity of the matrix.

Finally we take a porosity dependence of η given by the exponential form

$$\eta(\phi) = \eta_0 e^{-\lambda(\phi - \phi_0)}, \tag{4}$$

with constants η_0, ϕ_0 and λ (≈ 27) and assume bulk viscosity $\xi(\phi)$ can be related to η as

$$\xi(\phi) = r_\xi \eta(\phi), \tag{5}$$

where r_ξ takes a constant value $r_\xi = 5/3$.

2.3 Background flow and scaling

We consider a background flow of two dimensional simple-shear in an infinite domain, with velocity

$$\boldsymbol{v} = (\dot{\gamma}y, 0) \tag{6}$$

2

and uniform porosity, $\phi = \phi_0$ which we take as $\phi_0 = 0.05$ for the extent of this paper. Here $\dot{\gamma}$ is the rate of simple-shear strain and the x and y axes are taken to be parallel and perpendicular to the (one-dimensional) shear plane, respectively, as shown in Figure 1. $\dot{\gamma}^{-1}$ provides a time scale for the flow, and a natural length scale is provided by the compaction length

$$\delta_c = \sqrt{\frac{(r_\xi + 4/3)\,\eta_0 K_0}{\eta^L}}, \tag{7}$$

which defines a length scale over which compaction pressure transmits information about physical disturbances in the medium. With these scales and the previous reference parameters we introduce scaled variables as follows:

$$\begin{cases} \boldsymbol{X} = \boldsymbol{x}/\delta_c \\ \boldsymbol{V} = \boldsymbol{v}/(\dot{\gamma}\delta_c) \\ \mathbf{K}^* = \mathbf{K}/K_0 = (\phi/\phi_0)^n \mathbf{A} \\ P = (p^L - \rho\boldsymbol{g}\cdot\boldsymbol{x})/\eta_0\dot{\gamma} \\ \eta^* = \eta/\eta_0 = e^{-\lambda(\phi - \phi_0)} \\ \tau = \dot{\gamma}t \end{cases} \tag{8}$$

With respect to these scaled variables the equations of motion become

$$\frac{\partial\phi}{\partial\tau} = \nabla \cdot [(1-\phi)\boldsymbol{V}], \tag{9a}$$

$$\nabla \cdot \boldsymbol{V} = \frac{1}{r_\xi + 4/3}\nabla \cdot [(\phi/\phi_0)^n \mathbf{A}\nabla P], \tag{9b}$$

$$\nabla P = \nabla \cdot [\eta^*(\nabla\boldsymbol{V} + \nabla\boldsymbol{V}^T)] + \nabla[\eta^*(r_\xi - 2/3)\nabla\cdot\boldsymbol{V}], \tag{9c}$$

We further introduce the compaction rate $\mathcal{C} \equiv \nabla \cdot \boldsymbol{V}$, where a positive value of $\mathcal{C}$ corresponds to decompaction. It is clear that the background flow has no compaction (so porosity is constant) and no pressure gradients, so anisotropic permeability has no effect on the flow.

3   Formulation of anisotropic permeability

Suppose that an applied stress leads to melt pocket allignment as in Figure 1, where the σ_3-direction is the direction of maximum tensile stress. We make the modelling assumption that this form of MPO leads to an anisotropy in permeability such that permeability is low in the x'-direction and high in the y'-direction (as shown in Figure 1), and we define Θ as the angle between the x'-axis and the x-axis.

For this assumption, with respect to the x' and y' axes we have

$$\mathbf{A}' = \begin{pmatrix} \alpha & \gamma_1 \\ \gamma_2 & \beta \end{pmatrix} \tag{10}$$

where $\beta \geq 1$ and $0 \leq \alpha \leq 1$. A simple symmetry argument (provided in Appendix A) shows that $\mathbf{A}'$ should be diagonal and so we can set $\gamma_1 = \gamma_2 = 0$. Then, by using the rotation matrix

$$\mathbf{R} = \begin{pmatrix} \cos\Theta & -\sin\Theta \\ \sin\Theta & \cos\Theta \end{pmatrix}, \tag{11}$$

the anisotropy matrix in the continuum coordinates is written as

$$\mathbf{A} = \mathbf{R}\mathbf{A}'\mathbf{R}^T = \begin{pmatrix} \alpha\cos^2\Theta + \beta\sin^2\Theta & (\alpha-\beta)\cos\Theta\sin\Theta \\ (\alpha-\beta)\cos\Theta\sin\Theta & \alpha\sin^2\Theta + \beta\cos^2\Theta \end{pmatrix}. \tag{12}$$

4 Linear Stability Analysis

We consider the linear stability of sinusoidal perturbations of initial amplitude $\epsilon \ll 1$ imposed on the background flow given above. Hence we consider problem variables in the form:

$$
\begin{cases}
\phi = \phi_0 + \epsilon\phi_1\left(\boldsymbol{X}, \tau\right) \\
P = P_0 + \epsilon P_1\left(\boldsymbol{X}, \tau\right) \\
\boldsymbol{V} = \boldsymbol{V}^{(0)}\left(\boldsymbol{X}\right) + \epsilon\boldsymbol{V}^{(1)}\left(\boldsymbol{X}, \tau\right) \\
\dot{\varepsilon}_{ij}^* = \dot{\varepsilon}_{ij}^{(0)}\left(\boldsymbol{X}\right) + \epsilon\dot{\varepsilon}_{ij}^{(1)}\left(\boldsymbol{X}, \tau\right) \\
\mathcal{C} = \mathcal{C}_0 + \epsilon\mathcal{C}_1\left(\boldsymbol{X}, \tau\right)
\end{cases}
\tag{13}
$$

where the first term with index 0 represents the base-state flow of order one and the second term with index 1 represents the perturbation of order ϵ caused by $\epsilon\phi_1$. We can also Taylor expand $(\phi/\phi_0)^n$ and $e^{-\lambda(\phi-\phi_0)}$ to first order in ϵ as

$$
\begin{cases}
(\phi/\phi_0)^n = 1 + \epsilon n\phi_1/\phi_0 \\
e^{-\lambda(\phi-\phi_0)} = 1 - \epsilon\lambda\phi_1
\end{cases}
\tag{14}
$$

The base-state flow is

$$
\boldsymbol{V}^{(0)} = (Y, 0, 0),
\tag{15}
$$

with $\mathcal{C}_0 = 0$. Then the first order balance of equations (9b) and (9c) become

$$
\mathcal{C}_1 = \frac{1}{r_\xi + 4/3}\nabla \cdot [\mathbf{A}\nabla P_1]
\tag{16a}
$$

$$
\nabla P_1 = \nabla \cdot \left(\nabla\boldsymbol{V}^{(1)} + (\nabla\boldsymbol{V}^{(1)})^T\right) + (r_\xi - 2/3)\nabla\mathcal{C}_1 - \lambda\nabla \cdot \left[\phi_1\left(\nabla\boldsymbol{V}^{(0)} + (\nabla\boldsymbol{V}^{(0)})^T\right)\right]
\tag{16b}
$$

We consider porosity perturbations of the form

$$
\phi_1 = \exp\left[i\boldsymbol{\kappa} \cdot \left(\boldsymbol{x} - \int_0^\tau \boldsymbol{V}^{(0)}\mathrm{d}t\right) + s\left(\tau\right)\right]
\tag{17}
$$

where the wave-vector is $\boldsymbol{\kappa} = (\kappa_x, \kappa_y, 0) = \kappa\left(\sin\theta, \cos\theta, 0\right)$. Equation (17) represents harmonic waves moving passively in the base-state flow $\boldsymbol{V}^{(0)}$ with a time dependent log-amplitude s.

This linearised system can be solved, as in Appendix B, to obtain the growth rate

$$
\dot{s} = \lambda(r_\xi + 4/3)^{-1}\left(1 - \phi_0\right)\sin 2\theta\frac{\langle\boldsymbol{\kappa}, \mathbf{A}\boldsymbol{\kappa}\rangle}{1 + \langle\boldsymbol{\kappa}, \mathbf{A}\boldsymbol{\kappa}\rangle}.
\tag{18}
$$

Here we use the inner product notation,

$$
\langle\boldsymbol{\kappa}, \mathbf{A}\boldsymbol{\kappa}\rangle = \sum_i \sum_j \kappa_i A_{ij}\kappa_j.
\tag{19}
$$

For isotropic permeability, $\mathbf{A} = \mathbf{I}$, the growth rate is consistent with the instantaneous growth rate calculated by Spiegelman [2003] for isotropic permeability and viscosity. Further, note that if we take the limit $\kappa \to \infty$ the term involving $\mathbf{A}$ cancels and so we reduce to the isotropic case, while in the limit $\kappa \to 0$ the growth rate is zero. Hence, growth rate depends significantly on anisotropic permeability when $\kappa \sim 1$.

For a permeability matrix $\mathbf{A}$ of the form given in equation (12) we can calculate $\langle \boldsymbol{\kappa}, \mathbf{A}\boldsymbol{\kappa} \rangle$ explicitly as

$$\langle \boldsymbol{\kappa}, \mathbf{A}\boldsymbol{\kappa} \rangle = \kappa^2 \begin{pmatrix} \sin\theta & \cos\theta \end{pmatrix} \begin{pmatrix} \alpha\cos^2\Theta + \beta\sin^2\Theta & (\alpha-\beta)\cos\Theta\sin\Theta \\ (\alpha-\beta)\cos\Theta\sin\Theta & \alpha\sin^2\Theta + \beta\cos^2\Theta \end{pmatrix} \begin{pmatrix} \sin\theta \\ \cos\theta \end{pmatrix}$$

$$= \kappa^2 \left(\alpha\sin^2(\theta+\Theta) + \beta\cos^2(\theta+\Theta) \right) \tag{20}$$

Hence we are interested in the behaviour of the factor F that modifies the isotropic growth rate, given by

$$F = \frac{\kappa^2 \left(\alpha\sin^2(\theta+\Theta) + \beta\cos^2(\theta+\Theta) \right)}{1 + \kappa^2 \left(\alpha\sin^2(\theta+\Theta) + \beta\cos^2(\theta+\Theta) \right)}. \tag{21}$$

F depends on the relative sizes of the parameters α, β and κ. Since α is less than β we have a peak where $\theta + \Theta$ is a multiple of π and troughs where $\theta + \Theta$ is an odd multiple of $\pi/2$. The shape of these peaks and troughs depends on the relative parameter sizes. Figure 2 shows the dependence of F on these parameters. Firstly it shows that when κ is significantly greater or smaller than 1 the θ dependence is weak and so the growth rate is similar to the isotropic case, as observed above. Secondly, if $\alpha \ll \beta$ the troughs are deep whereas if α and β are both of order 1 then the θ dependence is weak and the anisotropy doesn't have a significant effect on the growth rate. In the extreme case that $\alpha = 0$ the troughs drop all the way down to the axis and so perturbations at an angle $\theta = 90° - \Theta$ have a growth rate of 0. This implies that bands would never spontaneously form perpendicular to the MPO direction.

(a) $\alpha = 0.01$, $\beta = 10$ **(b)** $\alpha = 0.5$, $\beta = 2$
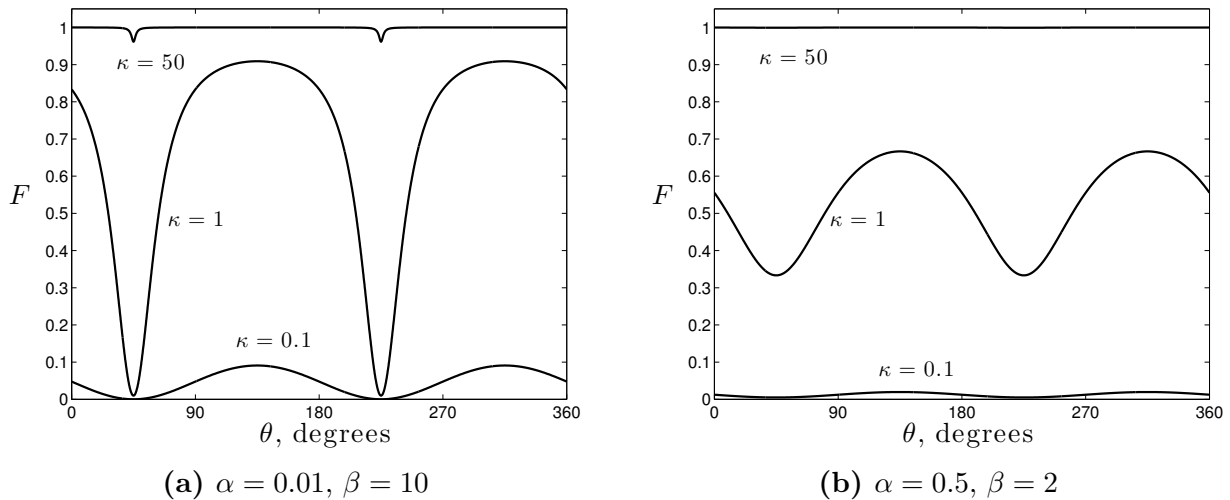
Figure 2: Anisotropy factor F, as a function of θ. In both cases $\Theta = 45°$.

4.1 Growth Rates and Low Angle Bands

In linear instability analysis, perturbations with the largest growth-rate will dominate the porosity distribution after a finite time and so we expect to observe high porosity bands forming at an angle, $\theta_{\max}$, corresponding to the perturbation angle with the largest growth-rate. Since we have shown that growth-rates depend strongly on the anisotropy for $\kappa \sim 1$, we take $\kappa = 1$ for the current section. We consider different values of κ in Section 4.2. Figure 3 shows a plot of growth-rate against θ for various values of the anisotropy angle Θ with $\alpha = 0.001$, and $\beta = 1.1$ which demonstrates that $\theta_{\max}$ depends on Θ.

In the case that $\Theta = 45°$ we see two peaks of equal growth rate, one lower than $45°$ and one higher, as demonstrated by $\Theta = 45°$ in Figure 3. Katz and Takei [2013] argue that although the
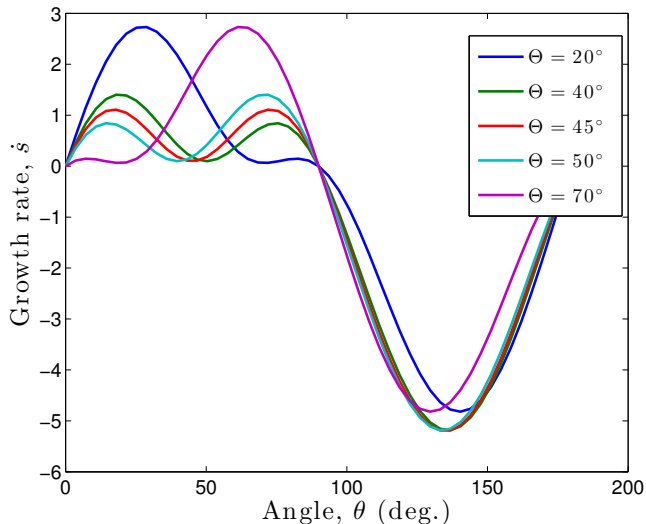
Figure 3: Growth-rate, $\dot{s}$, against θ for various values of anisotropy angle Θ. $\alpha = 0.01$, $\beta = 1.1$

two perturbations have the same growth rate, it is the lower angle perturbation that dominates, since the high angle band is rotated faster by the background flow until it reaches an angle at which it decays.

Since $0 \leq \alpha \leq 1$, $-\log(\alpha)$ lies in $(0, \infty)$ and is an appropriate measure of the magnitude of permeability decrease in the x' direction. Similarly $\log(\beta)$ is an appropriate measurement of permeability increase in the y' direction. Figure 4 gives contour plots of $\theta_{\max}$ (in degrees) for fixed $\kappa = 1$ against $-\log(\alpha)$ and $\log(\beta)$. Here, whenever there are multiple maxima, we take the smallest choice of $\theta_{\max}$, corresponding to bands that are rotated less quickly by the background flow. In these plots, the lower-left corner corresponds to the isotropic case (where $\theta_{\max} = 45°$) while the top-right corner corresponds to the case where MPO significantly decreases the permeability in the x' direction and also significantly increases it in the y' direction. Figure 4 demonstrates that $\theta_{\max}$ is furthest from $45°$ when there is strong permeability decrease in the x' direction but permability is relatively unchanged in the y' direction. Figure 4a is for $\Theta = 45°$ and shows that, if the other anisotropy parameters are of a particular form, $\theta_{\max}$ can be lowered to below $20°$, consistent with band angles observed in experiments. However these conditions are fairly restrictive and Figures 4b and 4c, for $\Theta = 20°$ and $\Theta = 70°$, demonstrate that for other anisotropy directions, $\theta_{\max}$ is not lowered to angles consistent with the experimental band angles.

4.2 Wavenumber Dependence

At the end of Section 4 we observed that anisotropic permeability has a significant effect on $\theta_{\max}$ when $\kappa \sim 1$ but not for large wavenumbers (small wavelengths). This is demonstrated well by Figure 5 which plots $\theta_{\max}$ against the logarithm of the wavelength for fixed anisotropy parameters. This plot includes $\theta_{\max} \geq 45°$ as well as the lower maximum and demonstrates that at wavelengths smaller than a tength of a compaction-length $\theta_{\max} = 45°$, as in the isotropic case.

Figure 6 shows growth rate against wavelength on a log-log scale for $\theta = \theta_{\max}$ and fixed anisotropy parameters. This figure demonstrates that growth rate is maximised at arbitrarily small wavelengths (high κ) and so, in fact, the dominant perturbations are not affected by anisotropic permeability. This suggests that anisotropic permeability may not be a contributing factor in low-angle band formation, however the instability of arbitrarily small wavelength perturbations is an unsatisfactory prediction of the model and certainly isn't observed in ex-

(a) $\Theta = 45°$

(b) $\Theta = 20°$

(c) $\Theta = 70°$
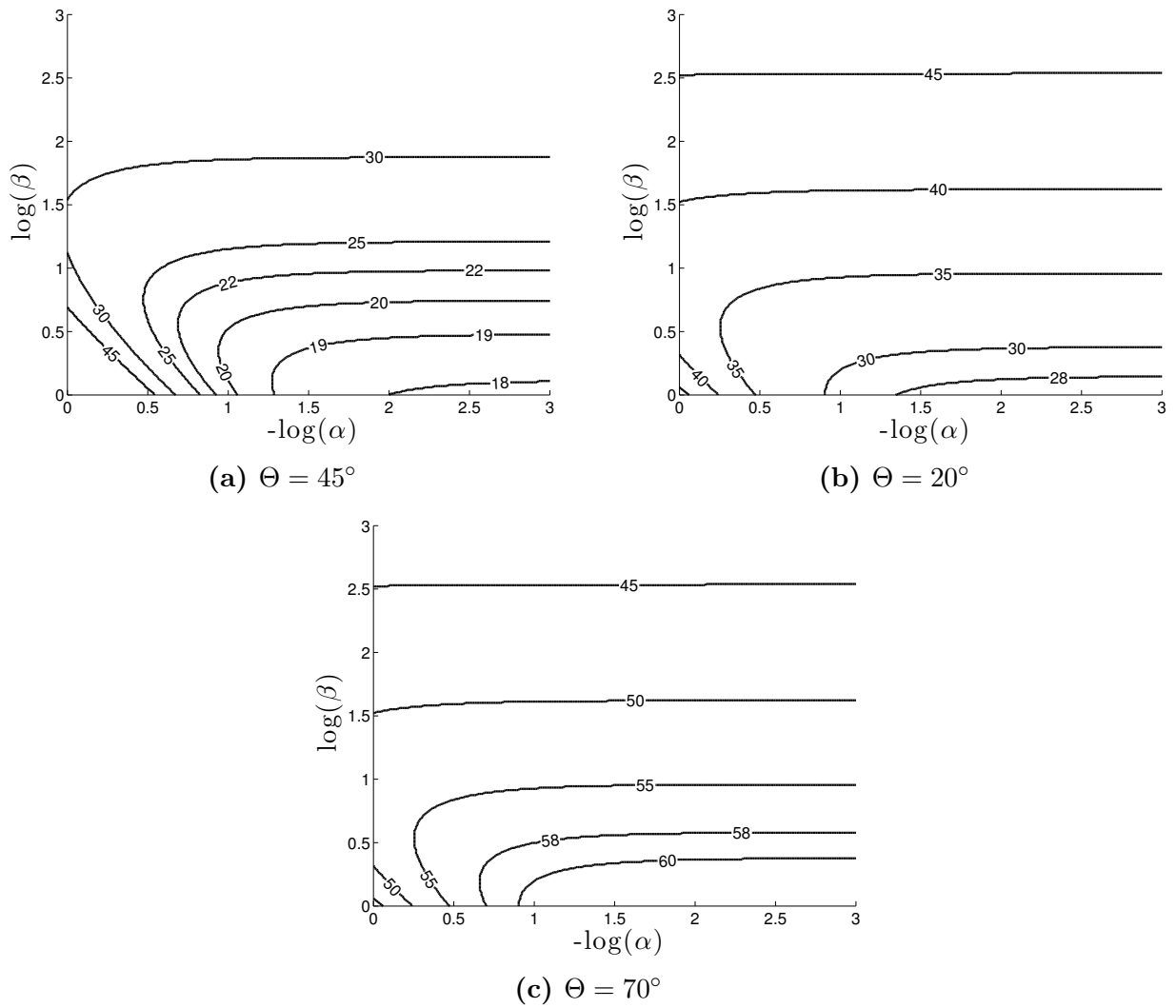
Figure 4: Contours of $\theta_{\max}$ in degrees against $-\log(\alpha)$ and $\log(\beta)$
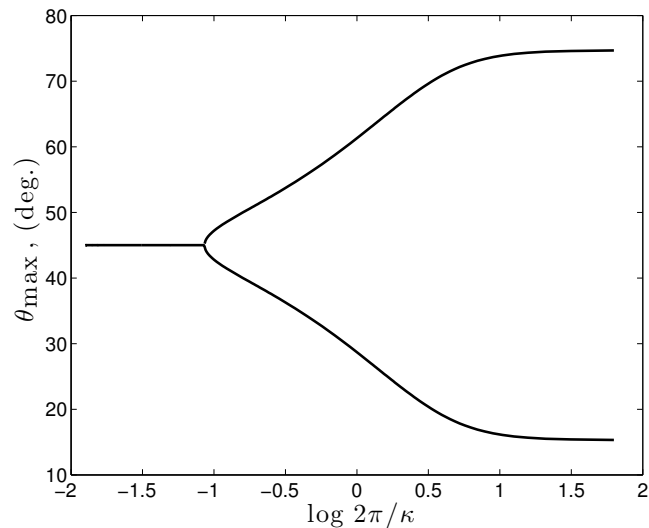
Figure 5: $\theta_{\max}$ against log-wavelength for $\Theta = 45°$, $\alpha = 0.01$ and $\beta = 1.1$

periments, so it is possible that some mechanism restricts the growth of these high wavenumber perturbations. These may come into play in the full non-linear system at finite time or through some regulating process not included in the model such as surface-energy or dissolu-

tion/precipitation.
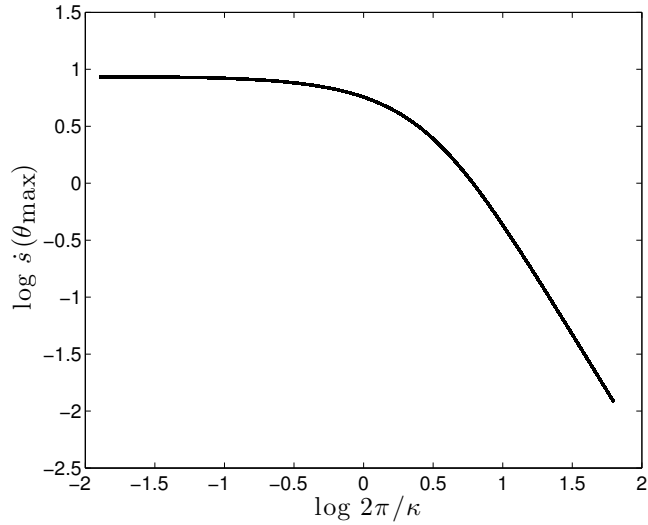
Figure 6: Maximum growth rate against wavelength for $\Theta = 45°$, $\alpha = 0.01$ and $\beta = 1.1$

5 Numerical Simulations

The previous analysis is linear and so does not necessarily apply to the behaviour of bands at finite strains. To investigate the effect of anisotropic permeability in the full non-linear model we numerically simulate a finite domain of the medium deforming under simple shear and apply a random porosity perturbation. Result from simulations with fixed anisotropy ($\alpha = 0.01, \beta = 1.1$ and $\Theta = 45°$) were compared to the results from simulations with isotropic permeability.

Since the analysis predicted different behaviours at different wavelength perturbations the initial porosity distribution was chosen to vary on different length scales. However the finite domain introduces an upper bound on these length scales. Furthermore the finite grid resolution introduces a lower bound since growth rates of short wavelength perturbation are suppressed. Fourier analysis was used to calculate the dominant wavelength and angle of the resulting porosity distribution. Predicted values of θ_{max} were calculated using Figure 5 and the dominant Fourier wavelength.

Simulation results are shown in Table 1 for isotropic and anisotropic media deformed to a strain of 0.25 for two different length scale perturbations. Visually the porosity distributions for isotropic and anisotropic permeability are very similar, however the angle spectrum indicates that anisotropy lowers the dominant band angle as predicted by the linear model. The angle was also lowered further for the porosity pertubation that varied on a larger length scale, consistent with the model. However the observed dominant band angle rarely corresponded exactly to the predicted θ_{max}. This could be due to boundary effects of the finite domain (since the linear analysis was performed for an infinite domain) or non-linear effects not incorporated in the analysis above. At higher strains porosity becomes close to 0 or 1 at which point the modelling assumptions become invalid and the numerical solvers tend to stop converging.

6 Discussion

In the analysis presented above, we have demonstrated the consequences of anisotropic permeability in the dynamics of a two-phase aggregate and specifically on its role in low-angle band

Isotropic	Anisotropic
$\theta_{\max} = 45°$	$\log(2\pi/\kappa) = -0.47 \implies \theta_{\max} = 36°$
$\theta_{\max} = 45°$	$\log(2\pi/\kappa) = 0.11 \implies \theta_{\max} = 27°$
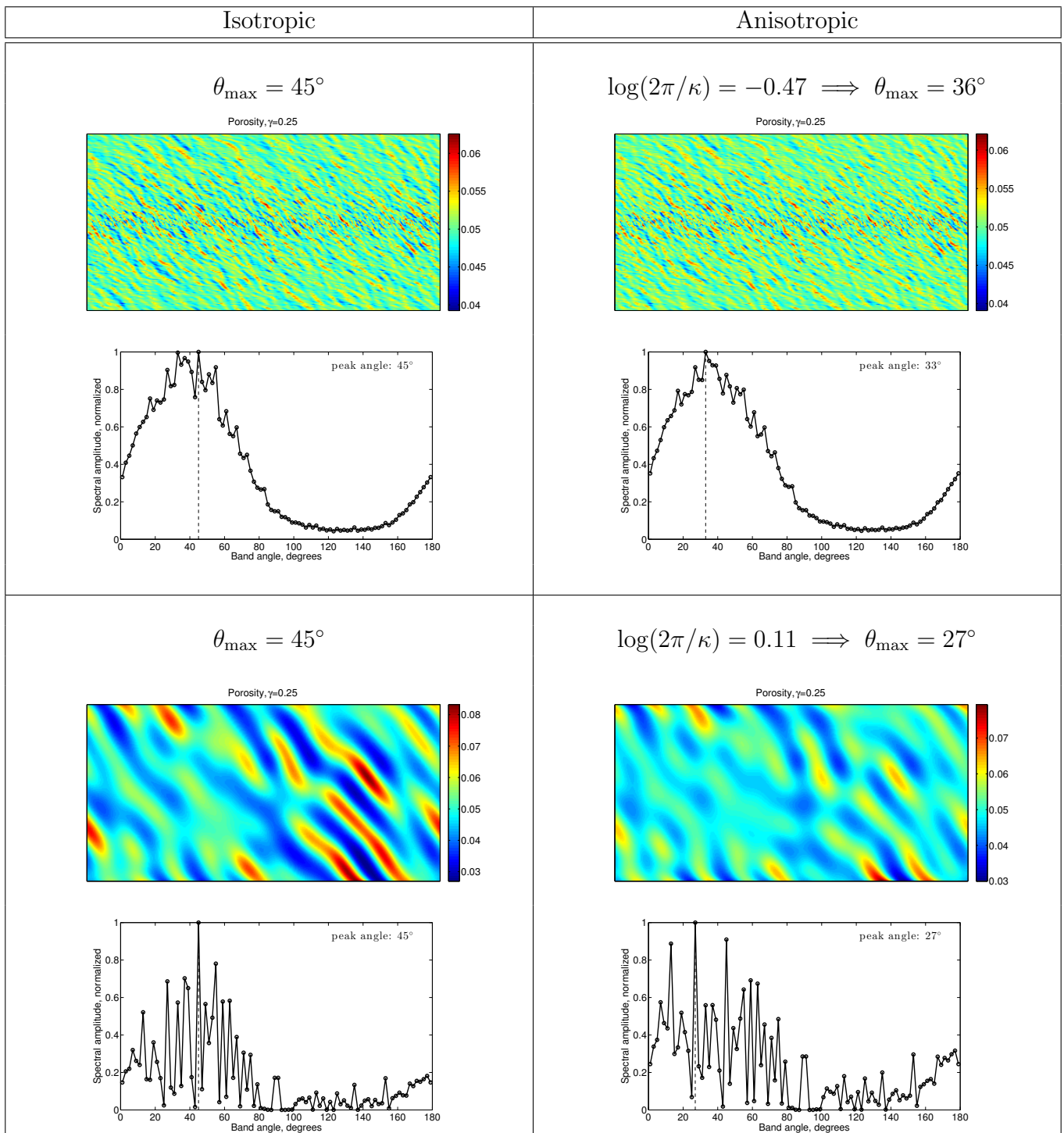
Table 1: Porosity distributions and angle spectra for two simulations at a shear of $\gamma = 0.25$. The anisotropic simulations were calculated with $\alpha = 0.01, \beta = 1.1$ and $\Theta = 45°$ as in Figure 5. Both simulations with isotropic permeability have a peak angle of $45°$. With anisotropy the peak angles are lower. The second porosity distribution varies on a greater length scale than the first and consequently has a lower peak angle in the Fourier spectrum. All simulations use a 400x200 grid.

formation in deformation under simple shear. We found that, at sufficiently large wavelengths, the angle to the shear plane of the fastest growing perturbations was consistent with band angles in experiments for a narrow range of anisotropy parameters. However this sensitivity to model parameters is inconsistent with the robustness of low band angle in laboratory experiments. Further, the analysis suggests arbitrarily short wavelength perturbations should be most unstable and dominate the resulting porosity distributions, this is unphysical and further

work should be done to address this problem.

In numerical simulations there was general qualitative agreement with the theory, such as bands forming at lower angles when the porosity perturbation varies on a length scale comparable to the compaction length. However, higher resolution simulations may be required to obtain greater quantitative agreement. The high porosities reached in numerical simulations are also unphysical and so a mechanism is required to prevent segregation occuring to this degree. Surface energy effects could help to explain these inconsistencies.

It is likely that some anisotropy in permeability arises due to MPO in partially molten rock deforming under shear. However, given the difficulty in obtaining maximal growth-rates for perturbations at an angle of $15 - 20°$ to the shear plane, it is unlikely that anisotropic permeability is a significant cause of low angle band formation as observed in experiments. It would be informative to test experimentally for anisotropic permeability in partially molten mantle rock deformed under shear, and attempt to measure the parameters α, β and Θ. New techniques for quantifying permeability in partially molten rock as used by Miller [2013] would make this possible.

7   Conclusion

Permeability of partially molten mantle rock is hypothesised to become anisotropic when the medium is deformed under shear. Anisotropic permeability is incorporated into the standard continuum model for partially molten rock and we investigate its impact on the band forming instability observed in experiments. A linear stability analysis found that band angles were generally lower than the $45°$ predicted in an isotropic model but that only a narrow range of parameters led to angles lower than $20°$ as consistently observed in experiments. This suggests this mechanism is not the driving factor in the formation of low angle bands.

Appendices

A   Argument for Diagonality of Permeability Tensor

Consider equation (1c) for a medium with uniform porosity, $\phi = \phi_0$, and neglect gravity:

$$\phi_0 \left(\boldsymbol{v}^S - \boldsymbol{v}^L \right) = \frac{K_0}{\eta^L} \mathbf{A} \nabla p^L. \tag{22}$$

With respect to the x' and y' axes this becomes

$$\boldsymbol{q} = \frac{K_0}{\phi_0 \eta^L} \begin{pmatrix} \alpha & \gamma_1 \\ \gamma_2 & \beta \end{pmatrix} \nabla p^L, \tag{23}$$

where $\boldsymbol{q} = \boldsymbol{v}^S - \boldsymbol{v}^L$ is segregation velocity. For a unit pressure gradient, $\nabla p^L = (0, 1)$, applied in the y'-direction we have segregation

$$\boldsymbol{q} = \frac{K_0}{\phi_0 \eta^L} (\gamma_1, \beta) \tag{24}$$

with an x'-component, $q_{x'}$, proportional to γ_1.

If we reflect in an axis parallel to the y'-direction, as shown in Figure 7, the pressure gradient is unchanged and the segregation becomes

$$\boldsymbol{q} = \frac{K_0}{\phi_0 \eta^L} (-\gamma_1, \beta) \tag{25}$$

with an x'-component, $q_{x'}$ proportional to $-\gamma_1$. However, the melt-pocket structure in Figure 1 is unchanged and so the permeability tensor should not change. Hence the segregation calculated by (23) is

$$\boldsymbol{q} = \frac{K_0}{\phi_0 \eta^L}(\gamma_1, \beta). \tag{26}$$

So we have $\gamma_1 = -\gamma_1 = 0$, and by a similar argument $\gamma_2 = 0$.
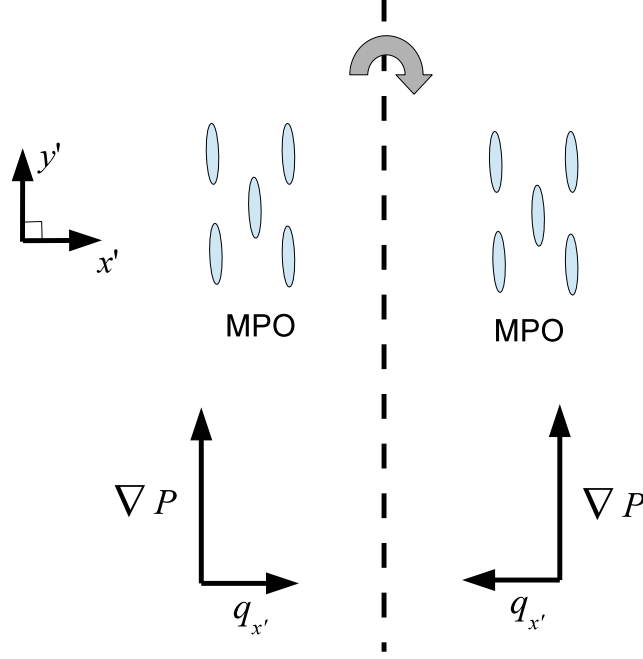
Figure 7: Reflection of MPO in y'–axis

B   Solving the Linearised Equations for Growth Rate $\dot{s}$

Since we have linearised the governing system, we are able to relate the other variables to ϕ_1 via

$$\boldsymbol{V}^{(1)} = \tilde{\boldsymbol{V}}\phi_1, \quad P_1 = \tilde{P}\phi_1. \tag{27}$$

From the order ϵ balance in equation (9a) we have

$$\frac{\partial \phi_1}{\partial \tau} = (1 - \phi_0)\, \tilde{\boldsymbol{V}} \cdot \nabla\phi_1 - \phi_1 \mathcal{C}_0^{\;\;0} - \boldsymbol{V}^{(0)} \cdot \nabla\phi_1. \tag{28}$$

From equation (17) we have

$$\nabla\phi_1 = i\boldsymbol{\kappa}\phi_1, \tag{29a}$$

$$\frac{\partial \phi_1}{\partial \tau} = \left(-i\boldsymbol{\kappa} \cdot \boldsymbol{V}^{(0)}(\tau) + \dot{s}\right)\phi_1. \tag{29b}$$

which, when substituted into equation (28) gives an equation for the growth rate

$$\dot{s} = (1 - \phi_0)\, i\boldsymbol{\kappa} \cdot \tilde{\boldsymbol{V}} = (1 - \phi_0)\, \mathcal{C}_1/\phi_1. \tag{30}$$

Substituting $\boldsymbol{V}^{(0)} = (Y, 0)$, $\boldsymbol{V}^{(1)} = \tilde{\boldsymbol{V}}\phi_1$ and $P_1 = \tilde{P}\phi_1$ into the x and y components of equation (16b) gives

$$\begin{cases} \tilde{P}\kappa_x = i\left[(r_\xi + 4/3)\,\kappa_x^2\tilde{V}_x + (r_\xi + 1/3)\,\kappa_x\kappa_y\tilde{V}_y + \kappa_y^2\tilde{V}_x\right] - \lambda\kappa_y, \\ \\ \tilde{P}\kappa_y = i\left[(r_\xi + 4/3)\,\kappa_y^2\tilde{V}_y + (r_\xi + 1/3)\,\kappa_x\kappa_y\tilde{V}_x + \kappa_x^2\tilde{V}_y\right] - \lambda\kappa_x, \end{cases} \tag{31}$$

11

which can be combined using $\kappa_x^2 + \kappa_y^2 = \kappa^2$ (κ_x times first equation plus κ_y times second) to obtain

$$
\begin{aligned}
\tilde{P} &= i\left(r_\xi + 4/3\right)\left(\kappa_x \tilde{V}_x + \kappa_y \tilde{V}_y\right) - 2\frac{\kappa_x \kappa_y}{\kappa^2}\lambda \\
&= \left(r_\xi + 4/3\right)\mathcal{C}_1/\phi_1 - \lambda \sin 2\theta.
\end{aligned} \tag{32}
$$

By substituting this equation into equation (16a) we obtain

$$
\begin{aligned}
\mathcal{C}_1 &= \frac{1}{r_\xi + 4/3}\nabla \cdot \left(i\tilde{P}\mathbf{A}\boldsymbol{\kappa}\phi_1\right) \\
&= -\frac{\tilde{P}}{r_\xi + 4/3}\langle\boldsymbol{\kappa}, \mathbf{A}\boldsymbol{\kappa}\rangle\,\phi_1 \\
&= -\langle\boldsymbol{\kappa}, \mathbf{A}\boldsymbol{\kappa}\rangle\,\mathcal{C}_1 + \frac{\lambda \sin 2\theta}{r_\xi + 4/3}\langle\boldsymbol{\kappa}, \mathbf{A}\boldsymbol{\kappa}\rangle\,\phi_1.
\end{aligned} \tag{33}
$$

Hence, using (30), we obtain the growth rate

$$
\dot{s} = \lambda(r_\xi + 4/3)^{-1}\left(1 - \phi_0\right)\sin 2\theta\frac{\langle\boldsymbol{\kappa}, \mathbf{A}\boldsymbol{\kappa}\rangle}{1 + \langle\boldsymbol{\kappa}, \mathbf{A}\boldsymbol{\kappa}\rangle}. \tag{34}
$$

References

R. F. Katz and Y. Takei. Consequences of viscous anisotropy in a deforming, two-phase aggregate: 1. governing equations and linearised analysis. *J. Fluid Mech.*, 2013.

D. King, M. Zimmerman, and D. Kohlstedt. Stress-driven melt segregation in partially molten olivine-rich rocks deformed in torsion. 51:21–42, 2010. doi: 10.1093/petrology/egp062.

K. Miller, W. Zhu, L. Montési, and G. Gaetani. Experimental quantification of permeability of partially molten mantle rock. *Earth Plan. Sci. Lett.*, 2013.

M. Spiegelman. Linear analysis of melt band formation by simple shear. *Geochemistry, Geophysics, Geosystems*, 2003.

Y. Takei and B. K. Holtzman. Viscous constitutive relations of solid-liquid composites in terms of grain boundary contiguity: 1. Grain boundary diffusion control model. *Journal of Geophysical Research: Solid Earth (1978–2012)*, 114(B6):B06205, June 2009.